

## Microstructural Controls on Elastic Anisotropy of Finely Laminated Mancos Shale

Matthew J. Ramos<sup>1,2,\*</sup>, D. Nicolas Espinoza<sup>2</sup>, Eric J. Goldfarb<sup>1</sup>, Nicola Tisato<sup>1</sup>, Stephen E. Laubach<sup>3</sup> and Carlos Torres-Verdín<sup>2</sup>

1. Jackson School of Geosciences, The University of Texas at Austin, 2305 Speedway, Austin, Texas 78712
2. Department of Petroleum and Geosystems Engineering, The University of Texas at Austin, 200 E. Dean Keeton St., Austin, Texas 78712
3. Bureau of Economic Geology, The University of Texas at Austin, 10611 Exploration Way, Austin, TX 78758

\* corresponding author: [matthew.ramos@utexas.edu](mailto:matthew.ramos@utexas.edu)

### Abstract

Shales commonly exhibit anisotropy in their elastic wave velocity, which directly impacts the accuracy of seismic imaging and their geomechanical response to drilling and completions. Anisotropy is often caused by mineralogical layering, fractures, and rock fabric (i.e. oriented grains and intrinsic anisotropy of clay sediments). However, the relative impact of each of these features on macroscopic shale properties is not well understood. We combined scanning electron microscopy (SEM) and X-ray micro-computed tomography (CT) to image the mineralogical and structural heterogeneity of Mancos Shale and converted the acquired CT and SEM images into heterogeneous 2D elastic models. We used wave propagation numerical simulations to understand the effects that layering and fractures have on elastic wave velocity anisotropy. Consistent  $V_p/V_s$  ratios around 1.46 for modeled and measured velocities validates SEM observations of a quartz-dominated shale lithology. CT-derived models containing layering and fractures exhibit 28.6% and 58.8% of the  $V_p$  and  $V_s$  anisotropy observed in the laboratory, whereas SEM derived models exhibit 74.5% and 73.2% of the anisotropy, respectively. The increased anisotropy of SEM-derived elastic models is a result of the ability of the SEM to discern individual mineral grains and microstructural features, whereas the CT models require the use of an effective medium theory to model variations of lithology. Overall, modeled wave propagation perpendicular to bedding more closely captures the experimental velocities than parallel to bedding. Therefore, sub-resolution rock fabric anisotropy likely accounts for the relatively larger velocity mismatch in the parallel direction, and is likely responsible for the decreased anisotropy in coarse rock models. Future modeling would require higher resolution images to structurally constrain these features and/or anisotropic elements to account for fabric anisotropy. Despite some limitations, our study provides a reliable procedure to estimate

anisotropy of dynamic mechanical properties of laminated shales using SEM and CT imaging combined with numerical simulation of wave propagation.

**Keywords:** Velocity Anisotropy, SEM and X-Ray CT Microstructural Modeling, VTI.

## **Introduction**

The directional dependence of elastic wave velocity in sedimentary rocks is governed by several lithological properties such as presence of layering, aligned fractures and discontinuities, and the intrinsic anisotropy of clay minerals and clay sediments (Gueguen and Palciauskas 1994, Mavko et al. 2009). The relative importance of each of these properties depends on the scale of investigation (Nur 1971, Lo et al. 1986, Vernik and Nur 1992, Rasolofosaon 1998, Sayers 2004, Valcke et al. 2006, Zoback 2007, Sone and Zoback 2013). For example, seismic-scale anisotropy is mostly a result of variations in bulk physical properties (mass density and elastic stiffness) in rock layers (10-100 m scale) and it is often associated with major changes in depositional environment (Sayers 2005, Anderson and Harris 2006). At a much smaller scale, individual clay minerals exhibit intrinsic crystallographic elastic anisotropy (Johnston and Christensen 1995). When clays are preferentially oriented during compaction and lithification of shales and other clay-rich rocks, clay-rich layers become an important contributor to velocity anisotropy at the seismic scale (Wang 2002, Dewhurst and Siggins 2006).

Structural diagenesis may also cause anisotropy (Siegesmund et al. 1996). Compaction-induced changes in grain orientation/aspect ratio can give rise to a distinct fabric and associated cleavage, and tectonic stresses can cause rock failure at several scales (Powell 1979, Laubach et al. 2010, Milliken and Reed 2010). Wave velocities have been shown to be higher in the direction parallel to rock fabric/cleavage and fractures, and lower in the direction orthogonal to these features (Nur 1971, Scott et al 1993, Ramos et al. 2017). Diagenetic healing (mineralization) of fractures can reduce their compliance and overall impact on anisotropy (Anders and Laubach 2014, Gale et al. 2014). Elastic nonlinearity can also manifest in velocity anisotropy when a rock is subjected to deviatoric stresses, which close favorably oriented compliant fractures, grain boundary pores, and other microstructural defects (Nur and Simmons 1969, Schwartz et al. 1994). Elastic nonlinearity is known to cause an otherwise isotropic rock to exhibit faster velocities in the direction of the maximum normal stress (Sinha and Kostek, 1996, Johnson and Rasolofosaon 1996, Winkler 1996, Sayers 2002, Fang et al. 2013, Ramos et al. 2018).

Although several studies have emphasized the importance of individual rock unit characteristics (such as layering, clay crystallographic anisotropy, rock fabric, fractures, and microstructural compliance) on velocity anisotropy, rarely do shales contain only one of these features. Furthermore, such features are heterogeneously distributed throughout the rock. For example, a number of shales exhibit mm- to cm-thick clay-rich laminations, however during deposition of these layers, the unlithified sediments are often reworked and mixed with other fine-grained material by bottom currents (Slatt and Abousleiman 2011). Over time, these fine laminations aggregate into meter thick packages that are compacted and develop a preferentially oriented fabric during burial (Birgenheier et al. 2017). The stratigraphic boundaries between these micro and macro-scale layers often act as planes of weakness. The mechanical stratigraphy induced by these lithologic variations may dictate the location and orientation of natural fractures (Laubach et al. 2009, Gale et al. 2014, Sosa-Massaro et al., 2017). Natural fractures and pore space may also be preferential sites for the growth of secondary minerals such as carbonate cements or clays, which could decrease or increase velocity anisotropy depending on their orientation.

The measured velocity anisotropy of shales is a cumulative response to all of the above lithological characteristics. In shales, fractures may be in subparallel sets at a high angle to bedding, but they also commonly occur parallel or subparallel to bedding (Hancock 1985, Gale et al. 2014). Thus, both sedimentary layering and fractures can potentially produce anisotropy in this configuration. Decoupling and quantifying their relative impacts on macroscopic rock anisotropy may be useful for revealing information about hydrocarbon-bearing formations. For example, changes in sonic anisotropy along a horizontal wellbore may be related to spatial variations in the degree of natural fracturing, where decreases in anisotropy may be linked to the presence of bed-normal fractures. Since bed-normal fractures are less likely to be sampled during coring of the vertical exploration well, the ability to quantify their sonic response and identify naturally fractured zones can have important implications for hydraulic fracturing and enhancing hydrocarbon production from shales reservoirs (Crampin 1985, Germanovich and Astakhov 2004, Suarez-Rivera et al. 2013, Bosziak et al. 2014, Laubach et al. 2016). Accurately determining the impact of these lithological features on dynamic elastic anisotropy may also provide a means for estimating their influence on the rock static mechanical response to the

change of stresses and large strains imposed during drilling and completions (Ramos et al. 2017, Ramos et al. 2018).

In this paper we present a combination of imaging and numerical simulations for analyzing the relative importance of lithologic characteristics such as mineralogical variability, layering, and the presence of bed-parallel fractures on the anisotropy of elastic wave velocity. First, we present laboratory measurements of Mancos Shale velocity anisotropy, and provide X-Ray micro-computed tomography (CT) and Scanning Electron Microscopy (SEM) images to highlight the mineralogical and structural features likely contributing to the measured anisotropy. We present methods for combining the information gained from CT and SEM imaging to construct velocity-mass density models, which account for the mineralogical and structural heterogeneity of Mancos Shale at several scales. We focus on the simulation of elastic wave propagation in the directions parallel and perpendicular to layering and/or fractures within the various models. We compare the simulation results to the laboratory measurements to quantify the relative contribution of the aforementioned lithologic features on the measured velocity anisotropy.

## **Mancos Shale Characterization**

### *Rock Samples*

Mancos Shale cylindrical samples were cored from quarried blocks with layering oriented at  $0^\circ$  (horizontal),  $45^\circ$  (oblique), and  $90^\circ$  (vertical) with respect to the flat end-faces (Figure 1). All samples were cut to approximately 2:1 length to diameter ratio (50 mm x 25 mm) and end face-ground to ensure parallelism for triaxial experiments and ultrasonic monitoring (ASTM-D7012-14). Ultrasonic velocities of oriented cores were measured at 1 MHz central frequency and are shown in Table 1. A thin section with 60  $\mu\text{m}$  thickness was prepared from a  $90^\circ$  sample representing a plane in the 2-3 directions, and allowed for SEM imaging and analysis of the distinctly light and dark colored layers within Mancos samples (Figure 2). An additional 25 mm diameter by 6.25 mm thick slice was cut from the rock adjacent to the thin section location for comparison to CT results. Although samples were cut with respect to the overall bed orientation, samples contain cross-bedding and heterogeneity at several scales, which may impact the assumption of vertical transverse isotropy (VTI) presented in the following section.

### Elastic Anisotropy

The elastic behavior of Mancos Shale can be approximated with a vertical transverse isotropy (VTI) model, where the axis of rotational symmetry is perpendicular to layering. A VTI medium can be described by five independent elastic stiffness coefficients. We calculate the stress-dependent stiffness parameters  $C_{ij}$  by measuring  $P$ -wave and perpendicularly oriented  $S$ -wave velocities on rock plugs with end-faces at  $0^\circ$ ,  $45^\circ$ , and  $90^\circ$  with respect to bedding, such that:

$$\begin{aligned}
 C_{11}(\underline{\underline{\sigma}}) &= \rho V_{P11}^2 \\
 C_{12}(\underline{\underline{\sigma}}) &= C_{11} - 2\rho V_{S11}^2, \\
 C_{33}(\underline{\underline{\sigma}}) &= \rho V_{P33}^2, \\
 C_{44}(\underline{\underline{\sigma}}) &= \rho V_{S3b}^2, \\
 C_{55}(\underline{\underline{\sigma}}) &= \rho V_{S3a}^2 \\
 2C_{66}(\underline{\underline{\sigma}}) &= C_{11} - C_{12}, \text{ and} \\
 C_{13}(\underline{\underline{\sigma}}) &= -\left(\frac{C_{44} + C_{55}}{2}\right) + \left(4\rho^2 V_{P45}^2 - 2\rho V_{P45} (C_{11} + C_{33} + C_{44} + C_{55})\right)^{1/2} \\
 &\quad + \left(C_{11} + \frac{C_{44} + C_{55}}{2}\right) \left(C_{33} + \frac{C_{44} + C_{55}}{2}\right)
 \end{aligned}$$

where  $\rho$  is the bulk mass density of the rock sample, and  $V$ 's are the  $P$ - and  $S$ -wave velocities in different directions. Directions 1 and 2 are in the plane of bedding, and direction 3 is perpendicular to bedding (Fig. 2A). Thomsen's parameters  $\varepsilon$ ,  $\gamma$ , and  $\delta$ , permit evaluating the degree of anisotropy based on relationships among coefficients  $C_{ij}$  (Thomsen 1986), namely,

$$\varepsilon = \frac{C_{11} - C_{33}}{2C_{33}},$$

$$\gamma = \frac{C_{66} - \left( \frac{C_{44} + C_{55}}{2} \right)}{C_{44} + C_{55}}, \text{ and}$$

$$\delta = \frac{\left( C_{13} - \frac{C_{44} + C_{55}}{2} \right)^2 - \left( C_{33} - \frac{C_{44} + C_{55}}{2} \right)^2}{C_{33} (2C_{33} - C_{44} + C_{55})},$$

where  $\varepsilon$  and  $\gamma$  respectively represent the degree of  $P$ - and  $S$ -wave anisotropy with respect to the symmetry axis, while the value of  $\delta$  represents the relative ellipticity of the wave front as it travels through the medium. For a VTI medium,  $C_{44} = C_{55}$ ; however, in order to account for potential deviation from a true VTI medium, these values are often calculated individually, and their average used to calculate  $C_{13}$ ,  $\gamma$ , and  $\delta$ .

Thomsen's parameters in Figure 1 emphasize the prominent  $P$ - and  $S$ -wave velocity anisotropy and nonlinearity of Mancos Shale prior to and during triaxial stress testing (Ramos et al. 2017). Figures 1-A to 1-C compare Thomsen's parameters for the set of unconfined plugs ( $0^\circ$ ,  $45^\circ$ , and  $90^\circ$ ) to sets of plugs subjected to constant confining stress (0.69, 3.45, and 6.9 MPa) and then loaded axially until failure. Anisotropy parameters tend to decrease with increasing deviatoric stress. For example,  $\varepsilon$  and  $\delta$  decrease by roughly 50% and  $\gamma$  decreases by almost 30% during deviatoric loading. The decrease in anisotropy with increasing deviatoric stress indicates that velocities perpendicular to bedding increase more upon stress loading than those parallel to bedding. This behavior supports previous observations that bed-parallel fractures and other compliant microstructural features play an important role in Mancos elastic anisotropy and nonlinearity (Chandler et al. 2016, Ramos et al. 2017, Ramos et al. 2018). For reference, Table 1 shows the velocity measurements and corresponding Thomsen's parameters for the set of unconfined Mancos plugs. The Appendix details the experimental methods used for CT and SEM imaging, while Table SII summarizes peak stresses for each test.

#### *Mineralogical Variations Measured from SEM*

In order to better understand the mechanisms contributing to velocity anisotropy of Mancos Shale and its stress-dependence, we examined samples at several scales. Mancos samples exhibit mm-thick dark and light colored layers at both the core and thin section scales, which are easily distinguished by the unaided eye (Figures 2-A and 2-B). We performed SEM

analyses to identify and quantify the mineralogy within each layer. SEM results show that the photographed light and dark variations in lithology correspond to predominantly quartz-rich and clay-rich (kaolinite, illite, and smectite) layers, respectively (Figure 2-C) (Grigg 2016). Diagenetic calcite cements are prominent in the quartz-rich facies and are also present to a lesser degree in the clay-rich facies, whereas dolomite and pyrite are slightly more abundant in the clay-rich facies. Albite and orthoclase are also present throughout the sample, but less abundant than other minerals. Although Mancos samples appear to have an overall laminated quartz-clay composition, dispersed clays (both grain-coating and pore-filling) are present within the quartz-rich layers, and the clay-rich layers contain an abundance of finer grained quartz. Table 2 summarizes the average mineralogical composition for the two endmembers (quartz-rich and clay-rich) facies in Mancos samples. The endmember compositions represent only 25% of the imaged scanline, whereas the remainder of the sample is comprised of an intermediate composition with almost equal parts of clay and quartz.

#### *Structural Variability from X-Ray Micro-Computed Tomography*

X-Ray micro-computed tomography (CT) images provide insight into the degree to which variations in lithology (i.e. quartz- vs clay-rich layers) relate to variations in X-ray attenuation/transmission (CT number), which depends on mass density. Comparison between a photograph and a 13  $\mu\text{m}$  resolution CT image of a Mancos sample shows that the light colored and quartz-rich facies generally appears slightly duller (lower CT number) than the darker colored and clay-rich layers (Figure 2-D). However, these dull quartz-rich layers are abundant in bright spots, whereas clay-rich layers exhibit fewer and smaller bright spots. Bright spots are possibly related to calcite and dolomite with a small amounts of pyrite, which have higher levels of X-ray attenuation (CT number), due to their higher mass densities. Because quartz and most of the clay minerals present in the sample are known to have very similar mineral densities, the background variation in CT number between the major facies might be due to variations in porosity or the relative abundance of denser secondary carbonate minerals. For example, clay-rich facies are marginally brighter than the quartz-rich facies. Therefore, the increased brightness could be due to a decrease in intergranular porosity with increasing clay content, or the increased amount of dolomite. SEM and CT imaging confirm the presence of fractures close to interfaces between the quartz-rich and clay-rich facies, and higher density of fractures in clay-rich layers than in quartz-rich layers (Figures 2-C and 2-D).

Figure 2-E shows a 5  $\mu\text{m}$  resolution CT scan of a sub-section of the same Mancos Shale sample in Figure 2-D, which reveals more details about the rock microstructure than images at 40  $\mu\text{m}$ . Figure 2-F shows annotations of a few key microstructural interpretations. First, the rock exhibits a distinct fabric due to the alignment of oriented grains, which in general appears to trend left to right in the image, with a slight counter-clockwise rotation when moving from the clay-rich facies in the left-center of the image to the quartz-rich facies surrounding it. Fractures within the rock also seem to re-orient due to the change in facies type and fabric orientation. Fractures appear to be more continuous in the clay-rich facies, whereas quartz-rich facies exhibit fractures which tend to end abruptly and appear as fabric-parallel fracture sets. The fractures also appear to re-orient around the carbonate-grains. Because Mancos Shale samples exhibit a distinct fabric, and the fabric appears to play an appreciable role in dictating micro-fracture orientation, it is likely that the fabric also contributes to the measured elastic wave velocity anisotropy.

## **Methods for Constructing Mineralogically and Structurally Heterogeneous Velocity**

### **Models**

#### *Combining SEM and CT Imaging Results*

The SEM and CT results were combined to construct mass density and velocity models which capture the mineralogical and structural heterogeneity of Mancos Shale samples. First, SEM Energy Dispersive X-Ray Spectroscopy (EDS) maps of major elements (Al, Ca, Fe, K, Mg, Na, and Si) were overlain to quantify mineralogy and identify mineralogical variations across the sample (Figure 3). SEM Back-scattered Electron detection (BSE) maps were also used to differentiate between minerals with similar elemental compositions. Results were used to quantify the mineralogical compositions of the quartz-rich and clay-rich endmember facies. To test the impact of mineralogical variations on velocity anisotropy, a “Synthetic” layered model was constructed by populating a perfectly layered model with the mineralogical properties and volume fractions of the dominant facies (Table 2). This provided a baseline prior to adding the structural complexity from the CT imaging. Details of SEM and CT imaging are provided in the Appendix.

Several models were generated by using the imaged CT volumes as the model domain in order to preserve the spatial changes in lithology and structure. Figure 4 shows the workflow for transforming CT scans into density and then velocity models. Samples were scanned alongside

several objects with known density in order to help constrain the relationship between CT number and density (Figures 4-A and 4-B). The relationship between CT number and density was applied to each CT volume to generate maps of mass density (Figure 4-C). A density threshold was then used to spatially separate the two major facies (quartz- and clay-rich) (Figure 4-D). Effective mechanical properties of each layer (bulk and shear elastic moduli) were then estimated based on the SEM-derived mineralogical compositions, mineral moduli, and assumed values of grain aspect ratios to account for non-spherical grains such as clays (Table 2) (Berryman 2005). Individual mineral moduli represent average values of several reported values (Wang et al. 2001, Mavko et al 2009). Variations in aspect ratio did not have a noticeable impact on the model, thus conservatively estimated values of 1 and 0.1 were assigned to non-clay and clay minerals, respectively.

Due to the fine-grained nature of shales, it is impractical to discern and accurately segment shale grains from the pore space in CT images. Therefore, a segmentation-less method was used to account for porosity (bulk density) variations within the samples (Tisato and Spikes 2016, Goldfarb et al. 2017). A density-to-porosity conversion curve was used to estimate the porosity of each voxel from the CT-derived density maps. Air ( $0 \text{ kg/m}^3 = 100\%$  porosity) and dolomite ( $2870 \text{ kg/m}^3 = 0\%$  porosity) were used as lower and upper bounds for the conversion, respectively. A null porosity was assigned to any voxel with a higher mass density than dolomite. All voxels were assigned a porosity value and a mineralogical composition from either the quartz- or clay-rich layer endmembers. The Modified Voigt-Reuss-Hill (MVRH) effective medium theory was then applied to each voxel to adjust its effective shear and bulk moduli based on the estimated porosity (Hill 1952, Nur et al. 1998). The MVRH bulk and shear moduli were used to calculate the *P*- and *S*-wave velocities for each voxel within the CT volume (Figures 4-E and 4-F).

In addition to using the CT images as model domains, SEM images were also used to investigate wave propagation at a higher resolution. However, because many individual grains and pores were discernable in the SEM models, the MVRH model was not used. Instead the previously identified mineral grains were segmented and assigned reference values of density and velocities, and pores were treated as air (Table 2).

All CT and SEM models were constructed to capture the mineralogical and structural features (e.g. layering, fractures) that are presumed to contribute to the experimentally measured

*P*-wave velocity anisotropy (432 m/s) and the *S*-wave velocity anisotropy (242 m/s) of Mancos Shale (Table 3). Velocity anisotropy is defined as  $(V_{90^\circ} - V_{0^\circ}) / V_{0^\circ}$ , where  $V_{0^\circ}$  and  $V_{90^\circ}$  represent the wave velocities perpendicular and parallel to bedding, respectively. We simulated wave propagation perpendicular and parallel to these features in order to determine their impact on velocities and overall macroscopic anisotropy.

### *Wave Propagation Modeling*

Once mass density  $\rho$ ,  $V_p$ , and  $V_s$  models were constructed from the CT and SEM scans, elastic wave propagation was numerically simulated using the software Seismic mOdeling with FInite differences (SOFI-2D), which is a 2D viscoelastic time domain parallel code for modeling *P*- and *S*-wave propagation (Bohlen 2002). The finite differences code is 8<sup>th</sup> order in the time domain and 2<sup>nd</sup> order in the space domain, and explicitly solves for stress and particle velocity for each time step. In order to mimic the quartz piezoelectric transducers used to measure ultrasonic velocities in the laboratory, the seismic source and receiver elements in the SOFI-2D were placed within simulated endcaps that have the density and velocity properties of quartz (Figure 5). Each model was sub-divided into elements sized at the digital image resolution (e.g. 0.9  $\mu\text{m}$  for SEM-derived models), and models were surrounded by a 30 element thick air boundary to mimic the unconfined conditions. An attenuation factor of 8% was applied to the air boundaries (and 0% elsewhere) in order to dampen waves exiting the model domain and avoid reflections back into the area of interest. Elastic waves were simulated using a plane wave Ricker wavelet source function at a central frequency of 1 MHz (the central frequency of the ultrasonic transducers), and *P*- and *S*-waves were respectively mimicked by imposing vertical and horizontal displacements on the source elements, then we evaluated the seismograms of vertical and horizontal displacements recorded at the receiver elements. The seismograms for each simulation and wave type were merged together to represent an average wave trace and first arrivals were picked using an algorithm detecting changes in the slope of the seismogram. The sensitivity of the algorithm was adjusted for *S*-waves in order to avoid detecting the small amounts of *P*-wave noise present in the seismograms (Figure 5). We assume wave propagation behaves similar to the effective medium limit (long wavelength with respect to scale of heterogeneity) because all models have a resolution (element size) at least 100 times smaller than the wavelength (Backus 1962, Marion et al. 1994).

## Results and Analysis

### *Synthetic Layered Models*

Figure 5 shows the Synthetic model constructed to test the velocity anisotropy effects due to layering of endmember facies without structural variability. The  $V_p$  and  $V_s$  of the Synthetic models were 112% and 99% of the experimental velocities with bedding at  $0^\circ$ , and 100% and 93% with bedding at  $90^\circ$ , respectively (Table 3 and Figure 9). The Synthetic model also exhibited 13% and 48% of the experimental  $V_p$  and  $V_s$  anisotropy, respectively (Figure 10). The higher anisotropy in  $V_s$  than in  $V_p$  is likely due to the effective shear moduli of the quartz-rich facies being 7 GPa higher than clay-rich facies, whereas the effective bulk moduli of the two facies only differ by 0.1 GPa (Table 2). Overall, results from the Synthetic model show that our simple two facies model predicts velocities within 12% of the experimental measurements; however, these same results show just a 14.3% and 10.8%  $V_p$  and  $V_s$  anisotropy of the values measured in the laboratory, and therefore, it is unlikely that velocity anisotropy is caused solely (or even predominantly) by layering. Because this perfect layering alone could not reproduce the experimentally measured anisotropy, we also tested models which incorporated structural complexity such as the spatial variability of layer spacing and thickness observed in Mancos samples using CT imaging in the following section.

### *CT Models of Oriented Cores*

Figure 6 shows the  $V_p$  models of the Mancos Shale cores from which the experimental velocities were measured. These Core models were developed from 40  $\mu\text{m}$  resolution CT scans and the simulation results are shown in Table 3 and Figure 9.  $V_p$  and  $V_s$  of the Core models were 97% and 89% of the experimental velocities with bedding at  $0^\circ$ , and 86% and 81% with bedding at  $90^\circ$ , respectively (Table 3 and Figure 9). It is important to notice that the distinct color variations between the quartz-rich and clay-rich facies in Figure 2 do not necessarily relate to dramatic differences in density or velocity. Therefore, the resulting amount of velocity anisotropy from the model is fairly low, with  $V_p$  and  $V_s$  anisotropy being roughly 10% and 15.6% of those measured experimentally (Figure 10). Although the Core model exhibited relatively low anisotropy, the velocities in the  $0^\circ$  model were within 11% of the experimental values, but the  $90^\circ$  model were off by as much as 19%. Because the 40  $\mu\text{m}$  Core models did not capture the

experimental anisotropy, we tested smaller scale and higher resolution models to evaluate the impact of fractures and other microstructural features on the  $P$ - and  $S$ -wave velocities.

### *CT Models at 13 $\mu\text{m}$ Resolution Testing the Impacts of Layering and Fractures*

Figure 7-A shows the  $V_p$  map from the rock sample in Figure 2 derived from a CT scan at 13  $\mu\text{m}$  resolution. Figures 7-B, 7-C, and 7-D show the subsections of the sample tested to evaluate the impacts of layering and fractures on velocities and anisotropy at this higher resolution. The subsection in Figure 7-C shows model “13 $\mu\text{m}$ \_Layer”, which exhibits distinct bedding but does not have visible fractures. Contrary to the Core simulations, this model contains some distinctly oriented pores and visible carbonate cements. Despite the additional microstructural details captured at higher resolution,  $V_p$  and  $V_s$  of the 13 $\mu\text{m}$ \_Layer model were only 87% and 79% of the experimental velocities with bedding at 0°, and 77% and 72% with bedding at 90°, respectively (Table 3 and Figure 9). The resulting  $V_p$  and  $V_s$  anisotropy was 8.2% and 9.8% of the experimental values, which are the lowest of all our tested models.

Figure 7-D shows the “13 $\mu\text{m}$ \_Frac” model, which tested the impact of fractures by comparing wave propagation parallel and perpendicular to the prominent bed-parallel fractures. As expected, modeled velocities decreased with the addition of fractures.  $V_p$  and  $V_s$  were 76% and 74% of the experimental velocities with bedding/fractures at 0°, and 69% and 70% with bedding/fractures at 90°, respectively (Table 3 and Figure 9). Results show that  $V_p$  and  $V_s$  anisotropy increased, however, to 28.6% and 58.8% of the experimental measurements, indicating that fractures have an impact on velocity anisotropy, particularly for  $V_s$ . It should be noted that because fractures tend to form along bed boundaries, these anisotropy values are likely a combination of the effects of layering and fractures. Variations in fracture orientation would likely influence the measured anisotropy. Despite their seemingly open appearance in the 2D models, 3D volumes show that fractures faces often exhibit asperities, which have frictional stiffness. Fractures also exhibit finite strength, which allows samples to remain intact without confinement. Therefore, the fractures in the 13  $\mu\text{m}$  CT models were given the  $V_p$  and mass density of air (335 m/s, and 1.225 kg/m<sup>3</sup>), but a non-zero  $V_s$  (110 m/s) to account for fracture shear stiffness.

Figure 7-B shows model 13 $\mu$ m\_All, which captures most of the sample in Figure 7-A and incorporates both the layering and fractures in the 13 $\mu$ m\_Layer and 13 $\mu$ m\_Frac models. The resulting  $V_p$  and  $V_s$  increased to 88% and 80% of the experimental velocities with bedding/fractures at 0°, and 80% and 76% with bedding/fractures at 90°, respectively (Table 3 and Figure 9).  $V_p$  anisotropy decreased slightly from the 13 $\mu$ m\_Frac model (28.6%) to 25.4% and  $V_s$  anisotropy was roughly the same at 58.5% of the experimentally measured anisotropy. Overall the 13 $\mu$ m\_All model results show that incorporating both layering and fractures at higher resolution improves the accuracy of velocities and increases anisotropy. However, anisotropy measured from simulations is still significantly lower than the experimentally measured anisotropy.

#### *SEM Models at 0.9 $\mu$ m Resolution Testing the Impacts of Layering and Fractures*

Figure 8-A shows the 0.9  $\mu$ m SEM scan-line from which the models SEM\_Layer and SEM\_Frac were derived to test the impacts of layering and fractures, respectively. Figures 8-B to 8-E compare the mineralogy and  $V_p$  maps for the SEM-derived models. The unfractured SEM\_Layer model exhibited higher  $V_p$  and  $V_s$ , which were 117% and 113% of the experimental velocities with bedding at 0°, and 111% and 107% with bedding at 90°, respectively (Table 3 and Figure 9). The resulting  $V_p$  and  $V_s$  anisotropies were 58.3% and 49.8% of the experimental values, respectively. The  $V_p$  anisotropy was over twice as large as the highest value for the CT-derived models. However, the  $V_s$  anisotropy was lower than the 13 $\mu$ m\_Frac and 13 $\mu$ m\_All models, both of which were roughly 58.5%.

Figures 8-B and 8-C show the SEM\_Frac model, which exhibits a distinct fracture and some larger pores oriented relatively parallel to bedding. Model results show slightly lower  $V_p$  and  $V_s$  than the SEM\_Layer model with bedding/fractures at 0° (115% and 111% of the experimental velocities), and slightly higher  $V_p$  and  $V_s$  with bedding/fractures at 90° (114% and 109%), respectively (Table 3 and Figure 9). Furthermore,  $V_p$  and  $V_s$  anisotropy increased with the addition of fractures and was 74.5% and 73.2% of the laboratory measurements, respectively. Overall, SEM models exhibit the highest velocities, which were similar for the SEM\_Layer and SEM\_Frac models.  $V_p$  and  $V_s$  anisotropies also increased significantly for the SEM-derived models, particularly for SEM\_Frac, which included both layering and fractures.

## Discussion

### *Impact of Model Type on Velocities*

Modeled velocities in Table 3 and Figure 9 range between 69% and 117% of their equivalent experimental measurement. The focus of this study is not to match the absolute velocities but to evaluate velocity anisotropy. The relative error in velocities appears to be specific to the scale and type of the model tested. For example, the SEM models account for 3 of the 4 results with higher  $P$ -wave velocities than the experiments, and the Synthetic model is almost a perfect match parallel to bedding ( $90^\circ$ ), but is 112% of the experiment perpendicular to bedding ( $0^\circ$ ). In contrast to the SEM models, the CT derived models all exhibit lower velocities than those measured experimentally. Finally, we simulate wave propagation in 2D, which could also contribute to the velocity mismatch when compared to the 3D laboratory measurements.

SEM models provide the closest estimates of the  $V_p$  (14.3% error) and  $V_s$  (10.8% error) anisotropy measured in the laboratory. The increased anisotropy of the SEM models likely originate from two sources: the high resolution of the SEM (discussed in the next section) and the use of individual mineral properties (velocities and densities) rather than assuming a two endmember system. By identifying minerals and assigning their properties separately, the SEM models accounted for the small scale mineralogical and structural heterogeneity that was absent when using the average endmembers to represent the two facies in the CT models. Therefore, although CT models were able to capture the larger scale layering, the use of the two endmember facies hindered accounting for lithological variability.

Although results show a range of velocities from the various models, all of our simulations exhibit  $V_p / V_s$  ratios around 1.46, which is consistent with the experimental values of 1.43-1.48 (Figure 9). In the absence of fluids, changes in  $V_p / V_s$  ratio is related to lithology (Tatham, 1982, Castagna et al 1985, Mavko et al 2009). The relatively low  $V_p / V_s$  ratios observed are indicative of quartz-rich lithologies such as tight sandstones and siltstones (Mavko et al. 2009). This is consistent with our SEM analyses, which revealed that these rocks are extremely quartz-rich, even within the darker and more clay-rich layers. Therefore, the good match of  $V_p / V_s$  ratios provides validation for modeling and capturing the important lithologic characteristics that influence wave propagation in the laboratory.

### *Impact of SEM Model Resolution on Velocities*

The relatively high resolution of SEM-derived models allowed us to capture the intricate mineralogical layering, boundaries and orientations of major grains and large pores, and some micro-scale fractures. All of these features likely play a measurable role in the high velocity anisotropy of the SEM-derived models. Despite the relatively high resolution, many microstructural features were missed in the models. For example, the relatively fast velocities in the SEM models can be attributed partly to the inability of the SEM to image much of the existing micro-porosity at this resolution. Higher resolution SEM images exhibit porosity at grain boundaries and within the clay-rich layers, whereas the 0.9  $\mu\text{m}$  resolution SEM models show most grains in perfect contact with one another and only identify larger-scale pores and fractures. The stress dependence of velocities observed in the laboratory provides additional evidence for the important impact that these compliant grain boundaries and microfractures ( $< 5\mu\text{m}$  width) have on velocity anisotropy (Figure 1) (Anders et al. 2014). Although we did not incorporate much of the grain boundary porosity or microfractures in the numerical simulations, the mass densities of the SEM models were very similar to experimental measurements (Table 3). Therefore, the addition of these features (as porosity) would require increased density elsewhere in the model (i.e. unidentified denser mineral phases) to maintain a realistic overall mass density.

### *Impact of CT Model Resolution on Velocities*

The velocity mismatch between experiments and CT models increases with decreasing model size, increasing resolution, and more so with wave propagation in the direction parallel to bedding. For example, the 40  $\mu\text{m}$  resolution Core models are 22% closer to the experimental  $V_p$  than the 13 $\mu\text{m}$ \_Frac model. The increased velocity mismatch with decreasing model size is intuitive because the smaller models are less likely to capture the range of mineralogical and structural heterogeneity observed in Mancos Shale. This behavior is further evidenced by comparing the 13 $\mu\text{m}$  models. The smaller 13 $\mu\text{m}$ \_Frac model exhibited high anisotropy and lower velocities likely due to the disproportionate amount of fracture porosity and lack of higher velocity carbonates, respectively. The opposite is true for the 13 $\mu\text{m}$ \_Layer model, which exhibited high velocities but very little anisotropy. However, when these two models were incorporated into the 13 $\mu\text{m}$ \_All model, both higher velocities and increased anisotropy were preserved.

The decreased velocities in the higher resolution CT models could also point to limitations for estimating elastic properties using the segmentationless method and Modified Voigt-Reuss-Hill (MVRH) effective medium theory (Goldfarb et al. 2017). In the 40  $\mu\text{m}$  resolution Core model, MVRH successfully accounted for the lack of discernable porosity by modifying mechanical properties based on the calibrated CT-derived mass density (Figure 4). However, at a higher resolution some larger pores and fractures were visible and modeled as low velocity zones, which further decreased the overall velocity of the 13 $\mu\text{m}$  models. Additionally, the segmentationless method may be more accurate in monomineralic lithologies such as sandstone, where variations in density are associated directly with variations in porosity, rather than the complex variations in mineralogy observed in Mancos samples. Relating density variations with mineralogical changes is not straightforward, and the simplification of Mancos samples as having only two facies in our CT models could have also caused the decreased velocity results. For example, the higher resolution CT models highlighted the complex spatial variability of the carbonate minerals within the quartz- and clay-rich facies, which challenges the validity of our assumption of two dominant facies. Therefore, carbonates could potentially be modeled as their own facies, which would likely increase the overall velocities of the high resolution models. Despite the lower velocities at higher resolution, the ability to more accurately capture the lithological variability allowed the 13  $\mu\text{m}$  models to exhibit higher densities than the 40  $\mu\text{m}$  Core models, but still appreciably lower than the experimental, SEM, and Synthetic models (Table 3).

#### *Insights into the Controls on Shale Velocity Anisotropy*

The Synthetic and CT models results showed that layering alone contributes less than 13% of the experimentally measured  $V_p$  anisotropy. Furthermore, CT models capturing sample layering and fractures account for a maximum of 28.6% and 58.8% of the experimental  $P$ - and  $S$ -anisotropy, respectively. Therefore, the anisotropy of Mancos Shale is likely due to different microstructural features, including microfractures and clay-rich rock intrinsic anisotropy. Our SEM models showed the intricate mineralogical layering and micro-scale fractures associated with fabric, which resulted in higher amounts of anisotropy. Our CT models did not exhibit high enough resolution to capture these microstructural features, and higher resolution models would likely limit the application of the segmentationless method used in this study. In addition to the fabric and associated micro-fractures shown in Figure 2, the intrinsic anisotropy of oriented clays

also could not be captured with any of our models. Accounting for these features would likely have an appreciable impact on velocity results, particularly parallel to bedding, and may provide the answer to why our models exhibit lower anisotropy than the experimental measurements. However, directly capturing the structural distribution of fabric and micro-fractures in our models would require CT imaging at significantly higher resolutions. The orientation of fabric can also be estimated from high resolution SEM imaging or through use of X-ray texture goniometry (Valcke et al. 2006). Furthermore, accounting for rock fabric and the intrinsic anisotropy of layered clays would require wave propagation simulations which account for anisotropic elements that can discern fabric and clay intrinsic anisotropy. Such estimation could be obtained theoretically from the estimated orientation and abundance of the various clay mineral phases present in the sample (Mainprice and Humbert 1994, Mainprice et al. 2011).

## Conclusions

We utilized SEM and CT scanning to develop elastic models which honor the structural and mineralogical heterogeneity of Mancos Shale at several scales. The impacts of mineralogical layering and fractures on velocity anisotropy were investigated by simulating *P*- and *S*-wave propagation perpendicular and parallel to these features within each model. The following conclusions are a result of this work.

- A simplified mineralogy model consisting of two endmember facies (quartz-rich and clay-rich) is adequate for estimating velocities using CT-derived models at the core scale. However, CT-derived models at higher resolutions exhibit decreased accuracy, likely due to limitations in the segmentationless method when individual grains and pores are visible at high resolution. Furthermore, additional velocity error arises from converting variations in mass density into variations in lithology (just two facies) and thus variations of  $V_p$  and  $V_s$ .
- SEM scale models containing layering and fractures account for 74.5% and 73.2% of the experimentally measured *P*- and *S*-wave anisotropy compared to CT models which at most exhibit 28.6% and 58.8%, respectively. More detailed mapping of mineral phases and their spatial distribution likely caused SEM models to exhibit higher anisotropy than CT models.
- Modeled velocities ranged between 69% and 117% of their experimental equivalent. Large variations in model resolution (40 to 0.9  $\mu\text{m}$ ) and type (SEM vs CT) accounted for the

seemingly large range. Despite the velocity spread, modeled  $V_p / V_s$  ratios cluster around 1.46, consistent with the experimental values of 1.43-1.48 typical for quartz-rich rocks.

- Modeled wave propagation perpendicular to bedding more closely captures the experimental velocities than parallel to bedding. The cause for the relatively larger mismatch between modeled and measured velocities parallel to bedding and resulting in overall lower velocity anisotropy is likely the inability to model microstructural fabric (oriented clays and microfractures) and the intrinsic anisotropy of clays. Future modeling would require higher resolution images to structurally constrain these features and anisotropic elastic elements.
- The method described in this paper provides a new avenue for quantifying the relative impacts of rock microstructural features on velocity anisotropy and estimating rock mechanical properties using SEM and CT imaging combined with elastic wave numerical simulation.
- Potential new applications of the presented method include determining the impact of microfracturing in kerogen phases on dynamic rock properties and determining the impact of layering and fractures on quasi-static mechanical response at large strains.

## **Appendix: Experimental Methods**

### *SEM and CT Imaging*

A Zeiss Sigma Field Emission SEM with Back-scattered Electron detection (BSE) and Energy Dispersive X-Ray Spectroscopy (EDS) was used to image and map the elemental composition within the rock thin section. The BSE and EDS analyses were performed at 10 kV and a 120  $\mu\text{m}$  aperture was used for EDS mapping. Images were acquired using a 50  $\mu\text{s}$  dwell time for BSE and 2 minutes for EDS. Simultaneous BSE and EDS scanlines were collected through the center of the thin section. Scanlines were roughly 0.87 mm wide and spanned the entire 25 mm length in the direction perpendicular to bedding.

X-Ray micro-tomography (CT) imaging was performed using a Nikon XTH-225 scanner with a 225 kV micro-focus X-ray source and 3  $\mu\text{m}$  focal spot size. The 0°, 45°, and 90° samples were scanned upright at a resolution of roughly 40  $\mu\text{m}$ . The CT provides volume maps of X-ray energy transmission/absorption, which can be correlated to the density of the material being scanned, with CT number increasing with density. We assumed that these density changes

corresponded to variations in lithology and porosity, which allowed us to map major facies transitions and fractures within Mancos samples.

## **Acknowledgements**

This work was funded by the Statoil Fellows Program at the University of Texas at Austin awarded to M. J. Ramos in the Jackson School of Geosciences. We thank Bruce Hart and Tarun Grover from Statoil's shale assets team in Austin, Texas, for their guidance and support. Additional resources for CT imaging were provided by the Chevron Digital Petrophysics Laboratory at UT Austin. We also thank Sara Elliott and Stephanie R. Forstner from the FRAC consortium (<http://www.beg.utexas.edu/frac>) for assisting with SEM analyses. We are also thankful to the members of the Formation Evaluation Research Consortium at The University of Texas at Austin for their feedback on this work.

## **References**

- Anders, M.H., S.E. Laubach, and C.H. Scholz, 2014, Microfractures: A review. *Journal of Structural Geology*, **69**(B), 377-394.
- Anderson, D.S., and N.B. Harris, 2006, Integrated sequence stratigraphic and geochemical resource characterization of the lower Mancos Shale, Uinta Basin, Utah. *Utah Geological Survey*.
- ASTM International, 2014, Standard test methods for compressive strength and elastic moduli of intact rock core specimens under varying states of stress and temperatures. ASTM-D7012-14.
- Backus, G.E., 1962, Long-wave elastic anisotropy produced by horizontal layering. *Journal of Geophysical Research*, **67**(11), 4427-4440.
- Berryman, J.G., 1995, Mixture theories for rock properties. In *Rock Physics & Phase Relations*, T. J. Ahrens (Ed.)
- Birgenheier, L.P., B. Horton, A.D. Mccauley, C.L. Johnson, and A. Kennedy, 2017, A depositional model for offshore deposits of the lower Blue Gate Member, Mancos Shale, Uinta Basin, Utah, USA. *Sedimentology*, **64**, 1402-1438.

- Bodziak, R., K. Clemons, A. Stephens, and R. Meek, 2014, The role of seismic attributes in understanding the hydraulically fracturable limits and reservoir performance in shale reservoirs: An example from the Eagle Ford Shale, south Texas. *AAPG Bulletin*, **98**(11), 2217–2235.
- Bohlen, T., 2002, Parallel 3-D viscoelastic finite difference seismic modelling. *Computers and Geosciences*, 887-899.
- Castagna, J.P., M.L. Batzle, and R.L. Eastwood, 1985, Relationships between compressional-wave and shear-wave velocities in clastic silicate rocks. *Geophysics*, **50**(4), 571-581.
- Chandler, M.R., P.G. Meredith, N. Brantut, and B.R. Crawford, 2016, Fracture toughness anisotropy in shale. *Journal of Geophysical Research: Solid Earth*, **121**(3), 1706-1729.
- Crampin, S., 1985, Evaluation of anisotropy by shear-wave splitting. *Geophysics*, **50**(1), 142-152.
- Dewhurst, D.N., and A.F. Siggins, 2006, Impact of fabric, microcracks and stress field on shale anisotropy. *Geophysics Journal International*, **165**, 135-148.
- Fang, X., M. Fehler, Z. Zhu, T. Chen, S. Brown, A. Cheng, and M. N. Toksoz, 2013, An approach for predicting stress-induced anisotropy around a borehole. *Geophysics*, **78**(3), D143-D150.
- Gale, J. F. W., S. E. Laubach, J. E. Olson, P. Eichhubl, and A. Fall, 2014, Natural fractures in shale: a review and new observations. *AAPG Bulletin*, **98**(11), 2165-2216.
- Germanovich, L.N., and D.K. Astakhov, 2004, Fracture closure in extension and mechanical interaction of parallel joints. *Journal of Geophysical Research*, **109**(B2).
- Goldfarb, E.J., K. Ikelda, and N. Tisato, 2017, Segmentation-less digital rock physics using different effective medium theories, *SEG Technical Program Expanded Abstracts*, 3908-3913.
- Grigg, J.J., 2016, Macroscopic and microscopic controls on mechanical properties of mudstones. Master of Science Thesis, New Mexico Institute of Mining and Technology.
- Gueguen, Y. and V. Palciauskas, 1994, *Introduction to the physics of rocks*. Princeton University Press.

- Hancock, P.L., 1985, Brittle microtectonics: principles and practice. *Journal of Structural Geology*, **7**(3-4), 437-457.
- Hill, R. 1952, The elastic behavior of a crystalline aggregate. *Proceedings of the Physical Society, Section A* **65**, 349-354.
- Johnson, J.E., and N.I. Christensen, 1995, Seismic anisotropy of shales. *Journal of Geophysical Research*, **100**(B4), 5991-6003.
- Johnson, P.A., and P.N.J. Rasolofosaon, 1996, Nonlinear elasticity and stress-induced anisotropy in rock: *Journal of Geophysical Research*, **101**, 3113-3124.
- Laubach, S.E., J.E. Olson, M.R. Gross, 2009, Mechanical and fracture stratigraphy. *AAPG Bulletin*, **93**(11), 1413-1426.
- Laubach, S.E, P. Eichhubl, C. Hilgers, R.H. Lander, 2010, Structural diagenesis. *Journal of Structural Geology*, **32**(12), 1866-1872.
- Laubach, S.E., A. Fall, L.K. Copley, R. Marrett, and S. Wilkins, 2016, Fracture porosity creation and persistence in a basement-involved Laramide fold, Upper Cretaceous Frontier Formation, Green River Basin, U.S.A. *Geological Magazine* **153**(5/6), 887-910.
- Lo, T., K.B. Coyner, and M.N. Toksoz, 1986, Experimental determination of elastic anisotropy of Berea sandstone, Chicopee shale, and Chelmsford granite. *Geophysics*, **51**, 164-171.
- Mainprice, D., and M. Humbert, 1994, Methods of calculating petrophysical properties from lattice preferred orientation data. *Surveys in Geophysics*, **15**, 575-592.
- Mainprice, D., R. Hielscher, and H. Schaeben, 2011, Calculating anisotropic physical properties from texture data using the MTEX open-source package. *Geological Society of London, Special Publications*, **360**, 175-192.
- Marion, D., T. Mukerji, and G. Mavko, 1994, Scale effects on velocity dispersion: From ray to effective medium theories in stratified media. *Geophysics*, **59**(10), 1613-1619.
- Mavko, G., T. Mukerji, and J. Dvorkin, 2009, *The rock physics handbook: tools for seismic analysis of porous media*. 2nd edition: Cambridge University Press.

- Milliken, K.L., and R.M. Reed, 2010, Multiple causes of diagenetic fabric anisotropy in weakly consolidated mud, Nankai accretionary prism, IODP Expedition 316. *Journal of Structural Geology*, **32**(12), 1887-1898.
- Nur, A., and G. Simmons, 1969, Stress-induced velocity anisotropy in rocks: An experimental study: *Journal of Geophysical Research*, **74**, 6667-6674.
- Nur, A., 1971, Effects of stress on velocity anisotropy in rocks with cracks, *Journal of Geophysical Research*, **76**(8), 2022-2034.
- Nur, A., Mavko, G., Dvorkin, J., Galmudi, D., 1998, Critical porosity: a key to relating physical properties to porosity in rocks. *The Leading Edge*, **17**(3), 357-362.
- Powell, C. M., 1979, A morphological classification of rock cleavage. *Tectonophysics*, **58**(1-2), 21-34.
- Ramos, M.J., D.N. Espinoza, C. Torres-Verdin, K.T. Spikes, and S.E. Laubach, 2017, Stress-Dependent Dynamic-Static Transforms of Anisotropic Mancos Shale. *American Rock Mechanics Association*, 17-182.
- Ramos, M.J., D.N. Espinoza, S.E. Laubach, and C. Torres-Verdin, 2018, Quantifying static and dynamic stiffness anisotropy and nonlinearity in finely laminated shales: experimental measurement and modeling. *Geophysics* (Just Accepted).
- Rasolofosaon, P., 1998, Stress-induced seismic anisotropy revisited. *Oil & Gas Science and Technology - Rev. IFP*, **53**(5), 679-692.
- Sayers, C.M., 2002, Stress-dependent elastic anisotropy of sandstones. *Geophysical Prospecting*, **50**, 85-95.
- Sayers, C.M., 2004, Seismic anisotropy of shales: What determines the sign of Thomsen's delta parameter?. *SEG, Expanded Abstracts*, 103-106.
- Sayers, C.M., 2005, Seismic anisotropy of shales. *Geophysical Prospecting*, **53**, 667-676.
- Schwartz, L.M., W.F. Murphy III, and J.G. Berryman, 1994, Stress-induced transverse isotropy in rocks: *Society of Exploration Geophysicists Technical Program Expanded Abstracts*, 1081-1085.

- Scott, T.E., Jr., Q. Ma, and J.-C. Roegiers, 1993, Acoustic velocity changes during shear enhanced compaction of sandstone. *International Journal of Rock Mechanics and Mining Sciences & Geomechanics Abstracts*, **30**(7), 763–769.
- Siegesmund, S., J. H. Kruhl, and E. Lüschen, 1996, The significance of rock fabrics for the geological-interpretation of geophysical anisotropies. *Geotectonic Research*, **85**, 163 p.
- Sinha, B.K., and S. Kostek, 1996, Stress-induced azimuthal anisotropy in borehole flexural waves: *Geophysics*, **61**, 1899-1907.
- Slatt R.M., and Y. Abousleiman, 2011, Merging sequence stratigraphy and geomechanics for unconventional gas shales. *The Leading Edge*, **30**(3), 274-282.
- Sone, H., and M.D. Zoback, 2013, Mechanical properties of shale-gas reservoir rocks – Part 1: Static and dynamic elastic properties and anisotropy. *Geophysics*, **78**(5), D381-D392.
- Sosa-Massaró, A., Espinoza, D.N., Frydman, M., Barredo, S. and Cuervo, S., 2017. Analyzing a suitable elastic geomechanical model for Vaca Muerta Formation. *Journal of South American Earth Sciences*, **79**, 472-488.
- Suarez-Rivera, R., J. Burghardt, S. Stanchits, E. Edelman, and A. Surdi, 2013, Understanding the effect of rock fabric on fracture complexity for improving completion design and well performance. *International Petroleum Technology Conference*, 26-28 March, Beijing, China.
- Tatham, R.H., 1982,  $V_p/V_s$  and lithology. *Geophysics*, **47**(3), 336-344.
- Thomsen, L., 1986, Weak elastic anisotropy. *Geophysics* **51**, 1954-1966.
- Tisato, N., and K. Spikes, 2016, Computation of effective elastic properties from digital images without segmentation: 86th Annual International Meeting, SEG, Expanded Abstracts, 3256–3260.
- Valcke, S.L.A., M. Casey, G.E. Lloyd, J.-M. Kendall, and Q.J. Fisher, 2006, Lattice preferred orientation and seismic anisotropy in sedimentary rocks. *Geophysical Journal International*, **166**(2), 652-666.
- Vernik, L., and A. Nur, 1992, Ultrasonic velocity and anisotropy of hydrocarbon source rocks. *Geophysics*, **57**(5), 727-735.

- Wang, Z., H. Wang, M.E. Cates, 2001, Effective elastic properties of solid clays. *Geophysics*, **66**(2), 428-440.
- Wang, Z., 2002, Seismic anisotropy in sedimentary rocks, part 2: Laboratory data. *Geophysics*, **67**(5), 1423-1440.
- Winkler, K. W, 1996, Azimuthal velocity variations caused by borehole stress concentrations: *Journal of Geophysical Research*, **101**(B4), 8615-8621.
- Zoback, M.D. 2007, *Reservoir Geomechanics*. Cambridge University Press.

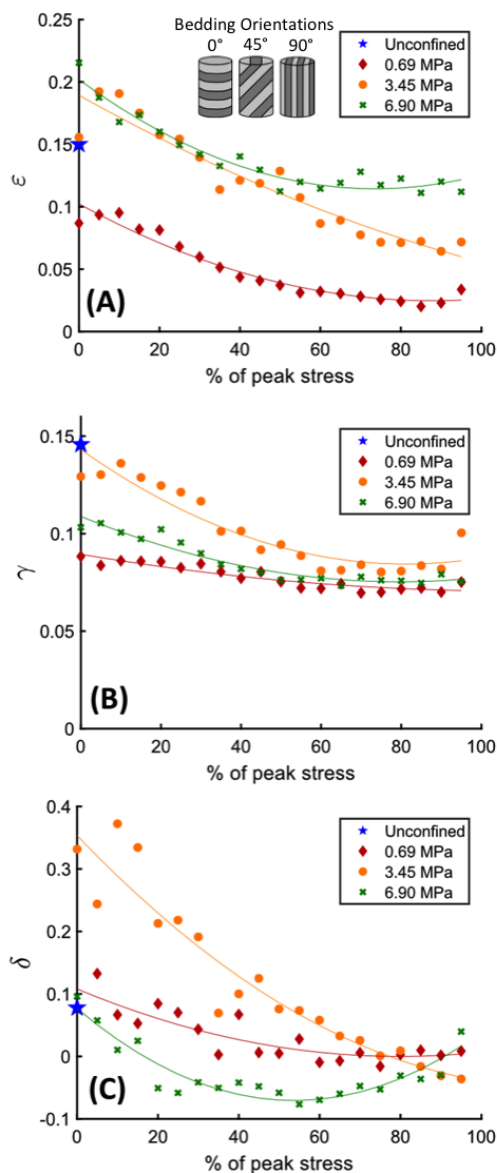


**Figure 1.** Experimentally determined Thomsen anisotropy parameters (A)  $\epsilon$ , (B)  $\gamma$ , and (C)  $\delta$  for Mancos Shale sample sets: unconfined (blue star), and subjected to a deviatoric stress loading path until failure with a constant confining stress of 0.69 MPa, 3.45 MPa, 6.9 MPa. Since Thomsen parameters are a combination of measurements from three oriented plugs (0°, 45°, and 90°) shown in A, they are calculated and plotted as a function of the % of peak stress for each test. Continuous lines represent best-fit approximations to the deviatoric stress dependence of Thomsen's parameters. Table S11 documents the peak stresses for each core orientation and confining stress.

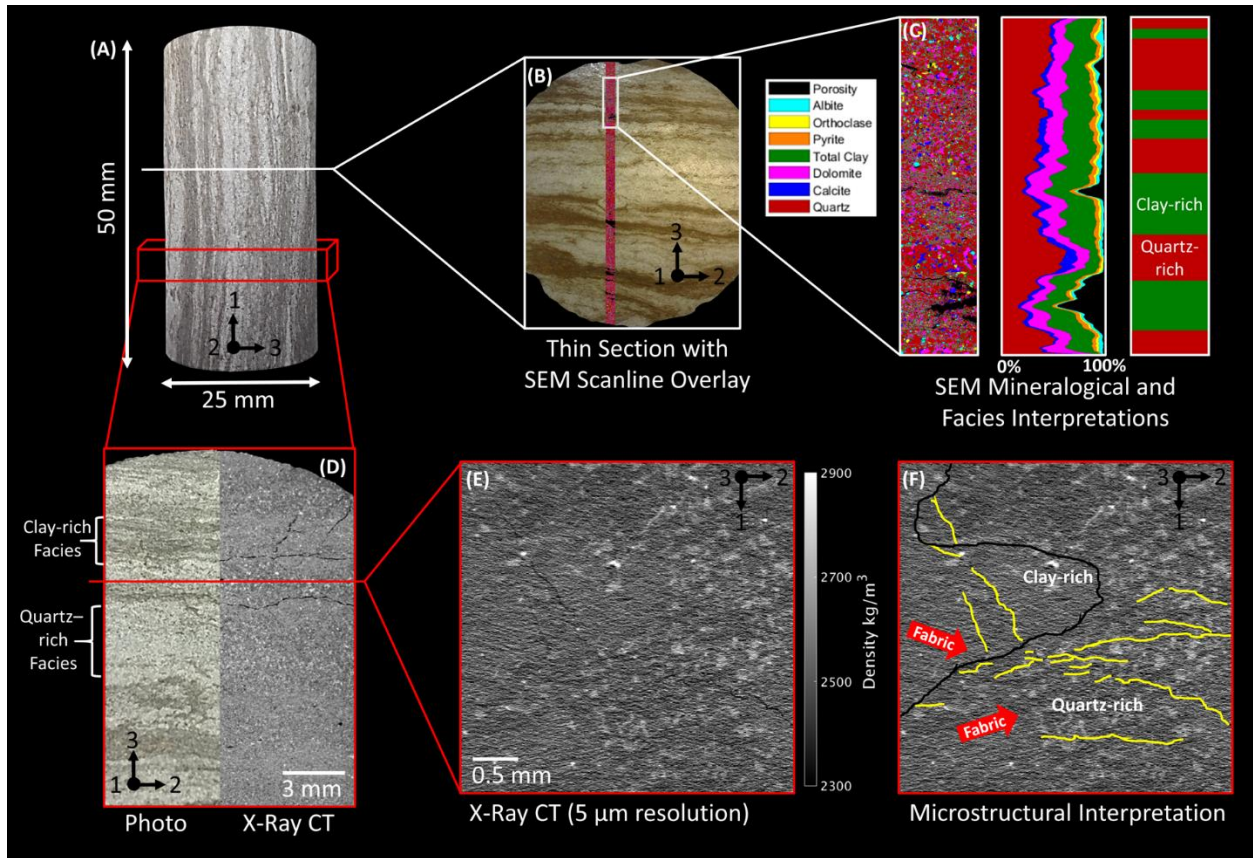


**Figure 2.** Evidence of layering, fractures, and rock fabric in the same Mancos sample at different scales. (A) Image of Mancos core with bedding at 90°, (B) photograph of thin section from center of the core with SEM scanline overlain (red), (C) sub-section of SEM scanline colored by the identified mineral phase, and associated mineralogy log showing volume fraction of minerals along the scanline, (D) comparison of photograph and 13  $\mu\text{m}$  resolution X-ray CT scan of the same sub-section of the core, (E) 5  $\mu\text{m}$  resolution X-ray CT scan, (F) annotated version of E, showing the interpreted facies boundary (black line), fabric direction (blue arrows), and interpreted fractures (yellow lines).

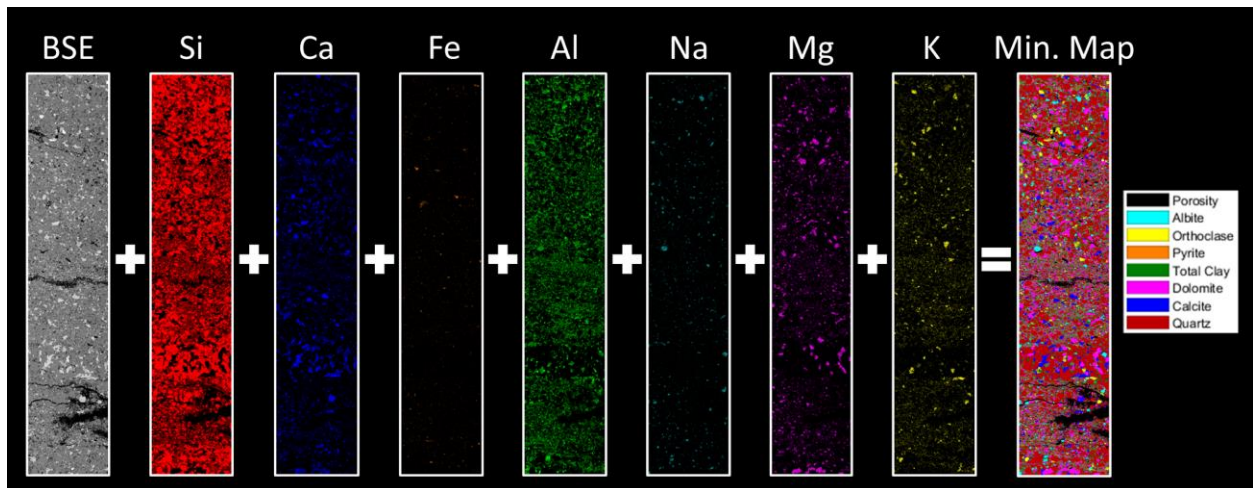


**Figure 3.** Workflow for determining mineralogy map (Min. Map) from SEM-derived Backscatter Electron (BSE) map and elemental maps of Silica (Si), Calcium (Ca), Iron (Fe), Aluminum (Al), Sodium (Na), Magnesium (Mg), and Potassium (K). Element maps were overlain to determine mineral locations, e.g. areas where Mg and Ca overlap were assumed to represent dolomite.

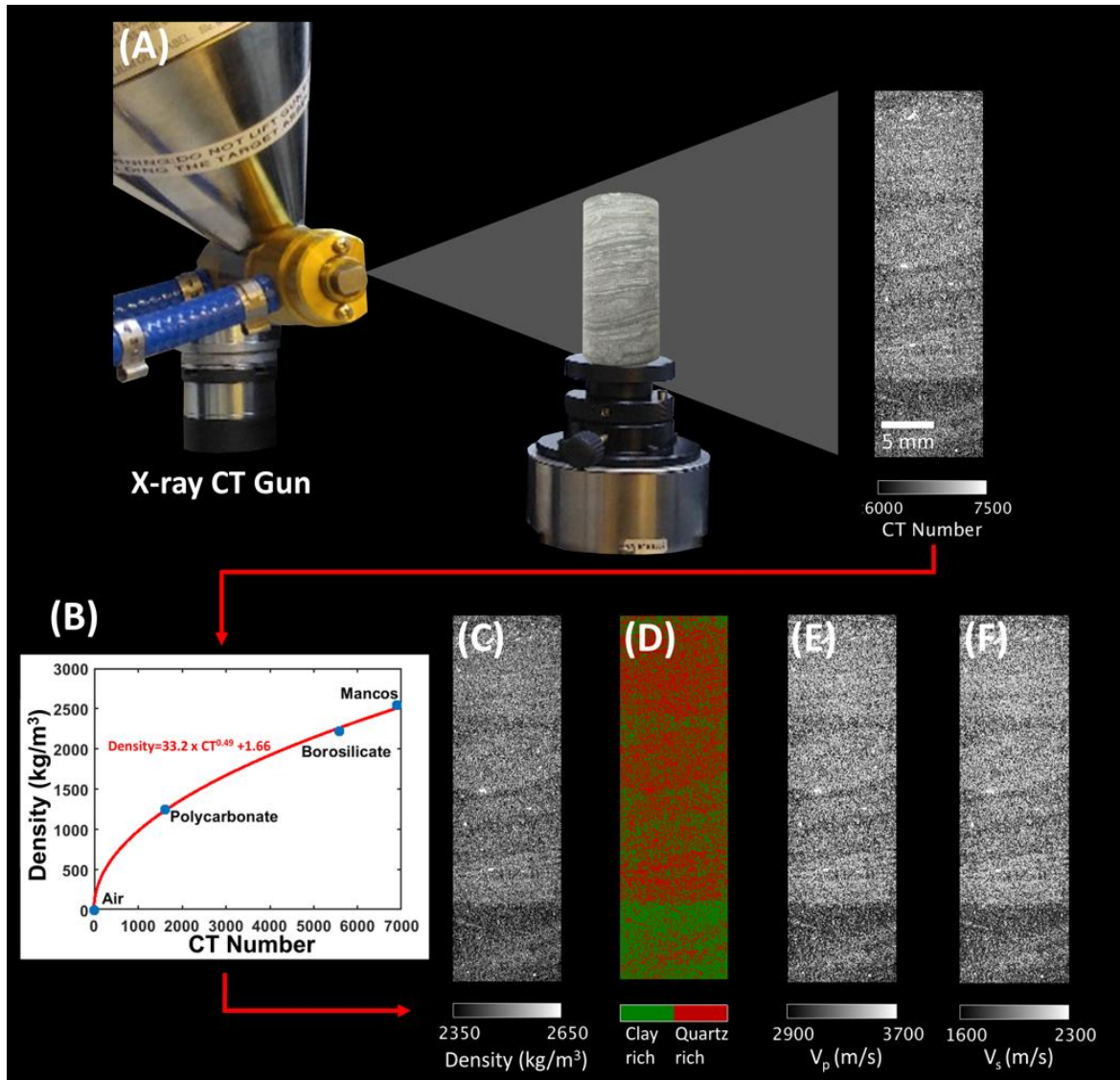


**Figure 4.** Workflow used for constructing velocity models from X-ray micro CT scans. (A) X-ray CT gun (left) scans sample (middle) resulting in the map of CT Number (right). (B) A relationship is developed between the average CT number and known density for the sample and reference objects (Air, Polycarbonate, and Borosilicate), which are also scanned with the sample. (C) A density map is generated from the map of CT number. (D) A cutoff density is selected to differentiate between the clay-rich (green) and quartz-rich (red) facies determined by SEM analyses. Average mineralogical compositions and associated elastic properties (Table 2) are assigned to each facies and scaled based on their relative density (porosity) using the Modified Voigt-Reuss-Hill effective medium theory to develop maps of elastic wave velocities (E)  $V_p$  and (F)  $V_s$ .

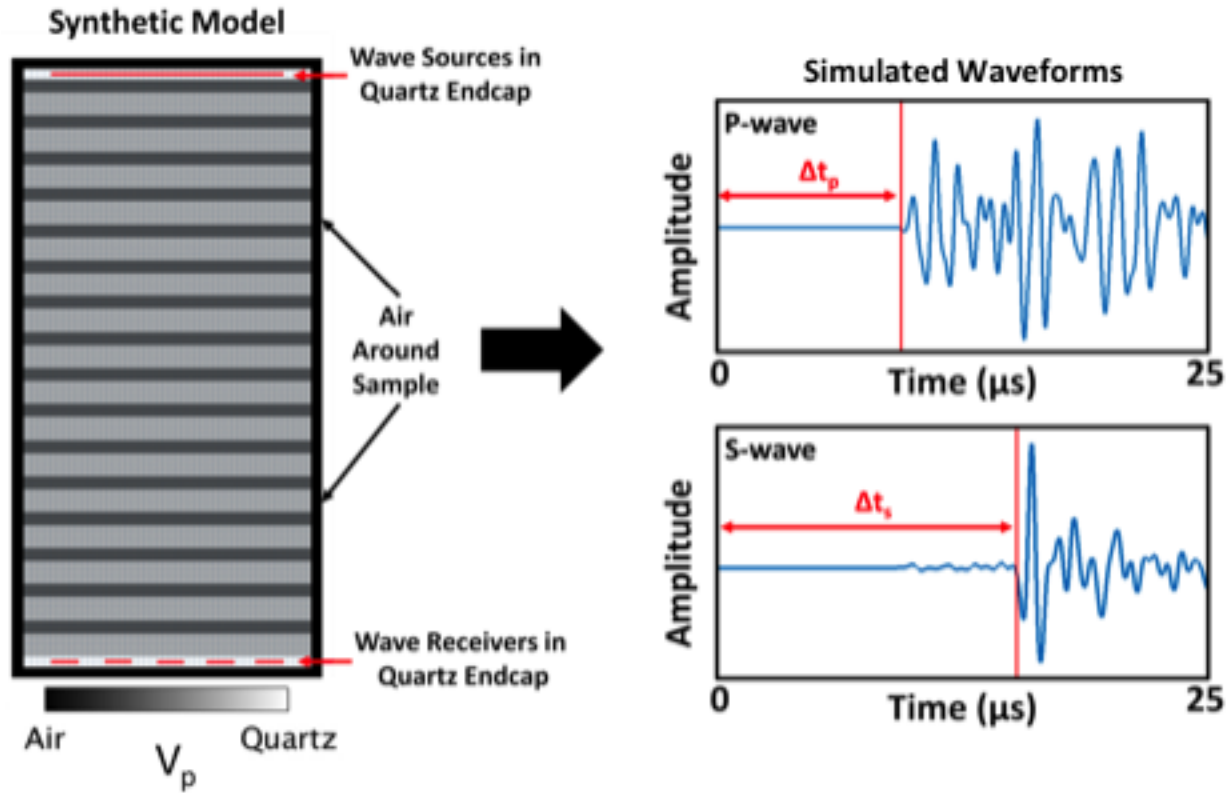


**Figure 5.** (Left) Example of the Synthetic  $V_p$  model with  $0^\circ$  bedding orientation and wave propagation perpendicular to bedding. Sources and receivers are placed in quartz endcaps in order to mimic the quartz piezoelectric transducers used in laboratory experiments, and the whole domain is surrounded by a wave-damping air boundary. Models are discretized to elements of size equal to the resolution of the images from which they are derived (i.e.  $40\ \mu\text{m}$  and  $13\ \mu\text{m}$  for CT models, and  $0.9\ \mu\text{m}$  for SEM models). (Right)  $P$ - and  $S$ -waveforms obtained from numerical simulations, with  $\Delta t$  representing the travel time for the wave through the sample before reaching the receivers. Velocities are calculated from travel times. All models are 2D approximations.

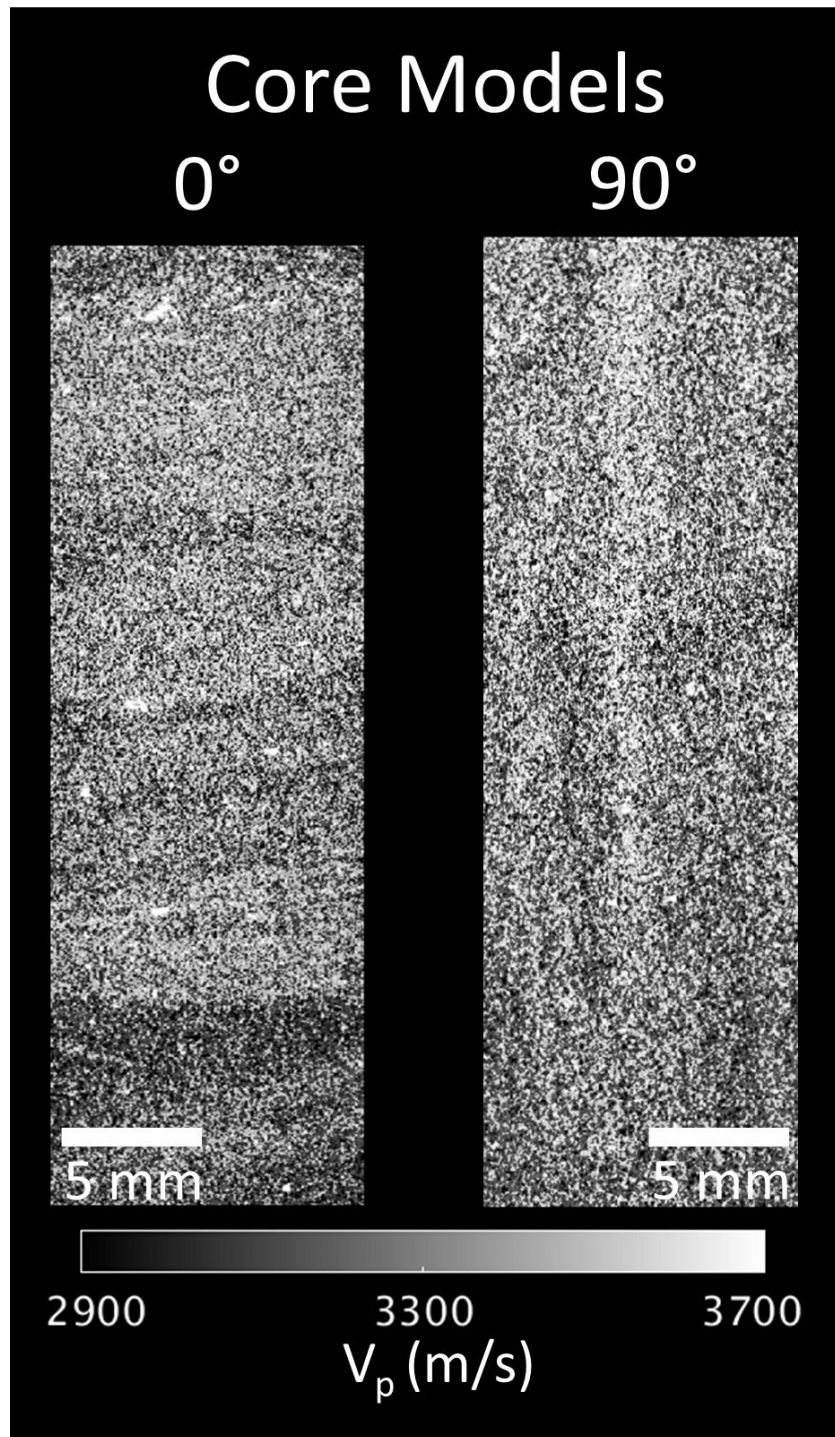


**Figure 6.** P-wave velocity models derived from 40  $\mu\text{m}$  resolution CT scan of Mancos Shale cores with bedding at  $0^\circ$  (left) and  $90^\circ$  (right). Model results listed in Table 3 as Core\_0° and Core\_90°.

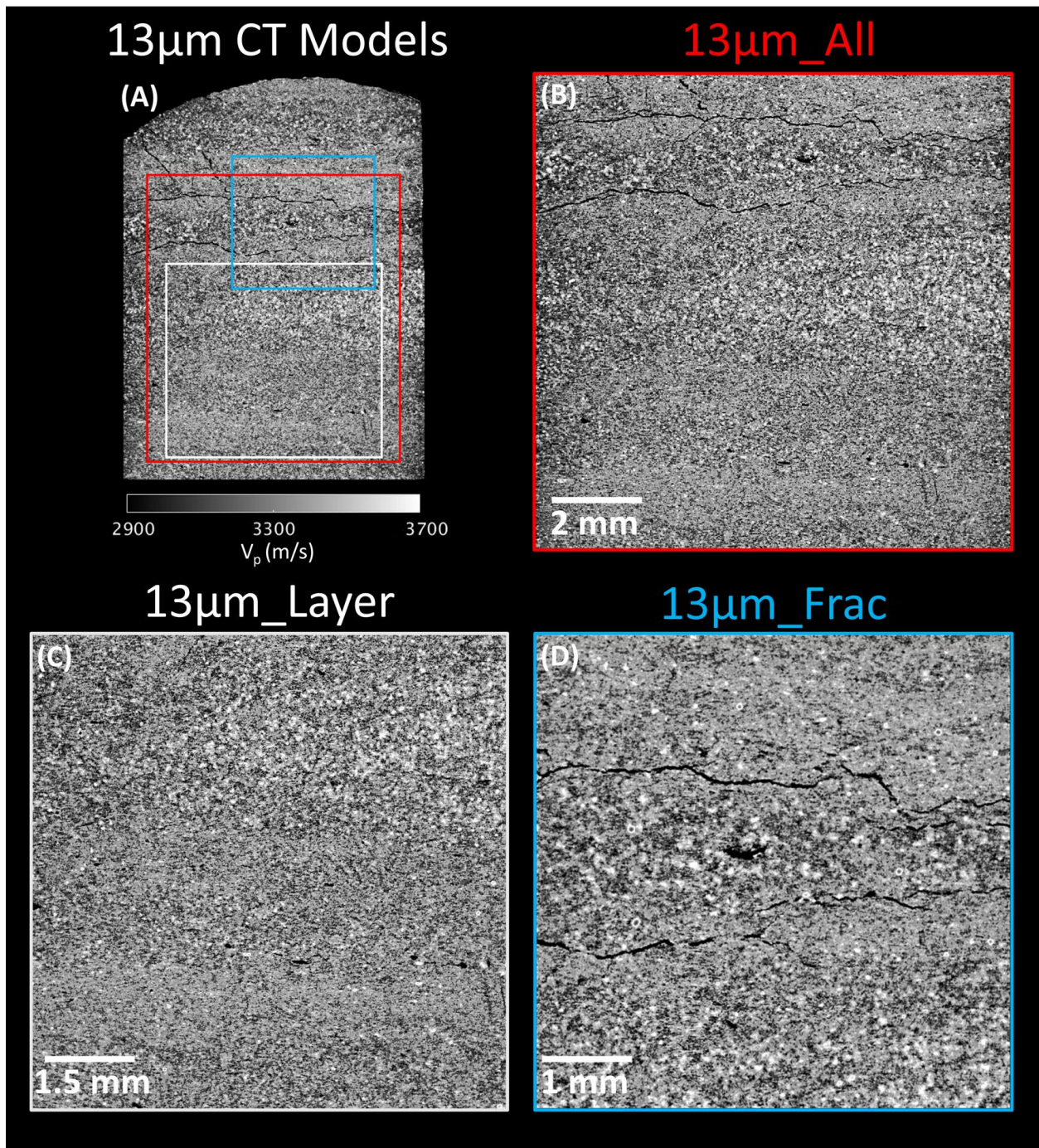


**Figure 7.** P-wave velocity models derived from 13 μm resolution CT scan of Mancos Shale shown in Figure 2-D. (A) Whole model from which subsections B-D were taken, (B) larger scale model to test the combined effects of C and D on velocity anisotropy (C) model used to test the impact of layering, and (D) model used to test the impact of fractures. Model results listed in Table 3 as 13μm\_All (B), 13μm\_Layer (C), and 13μm\_Frac (D).

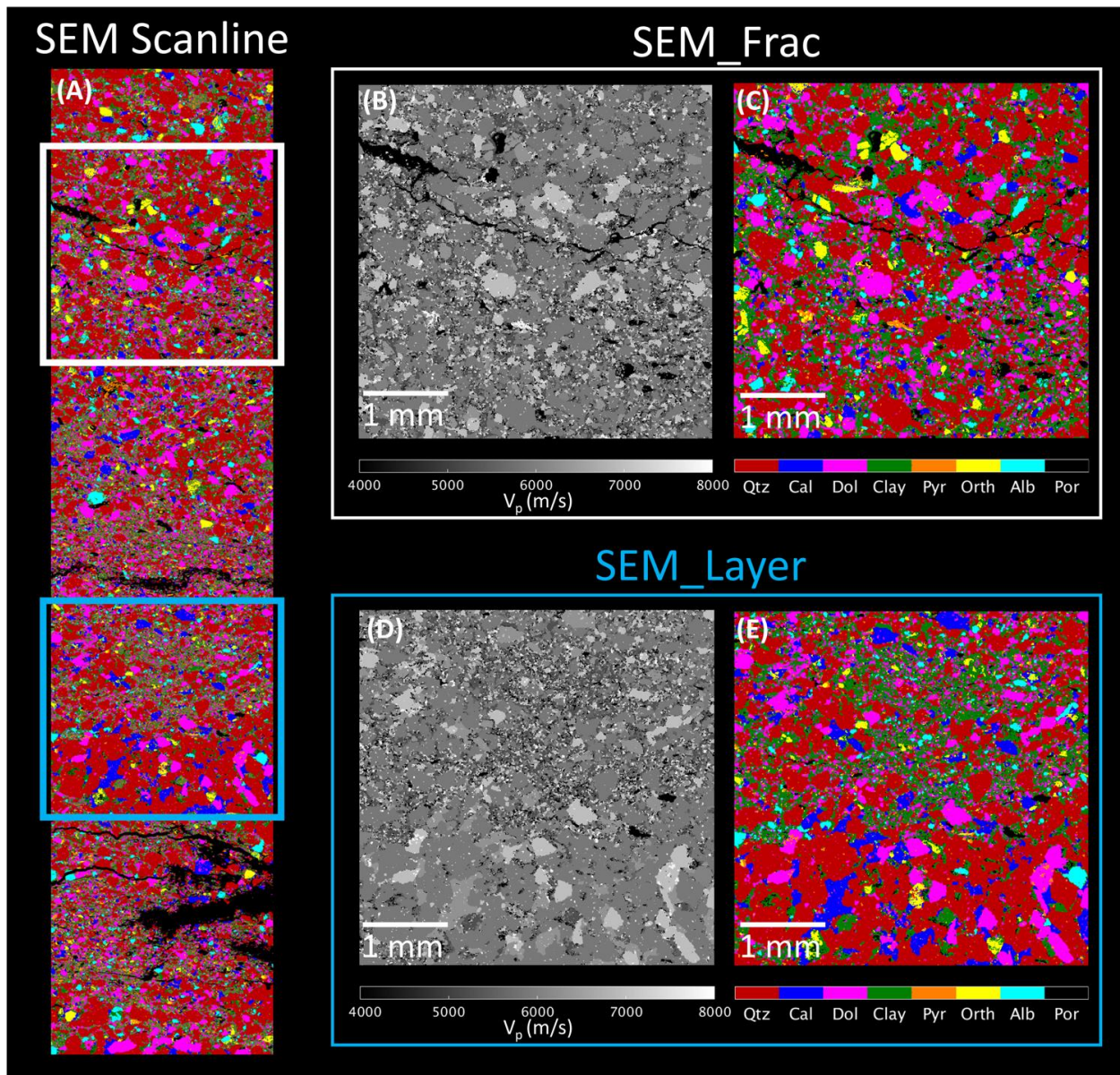


**Figure 8.** SEM minerology maps and P-wave velocity models derived from 0.9  $\mu\text{m}$  resolution SEM scanline shown in Figure 2.C. (A) Top of model from which subsections B-E were taken, (B)  $V_p$  model of SEM\_Frac used to test impact of fractures, (C) mineralogy map of SEM\_Frac, (D)  $V_p$  model of SEM\_Layer used to test the impact of layering, and (E) mineralogy map of SEM\_Layer. Model results listed in Table 3 as SEM\_Frac (B, C) and SEM\_Layer (D, E).

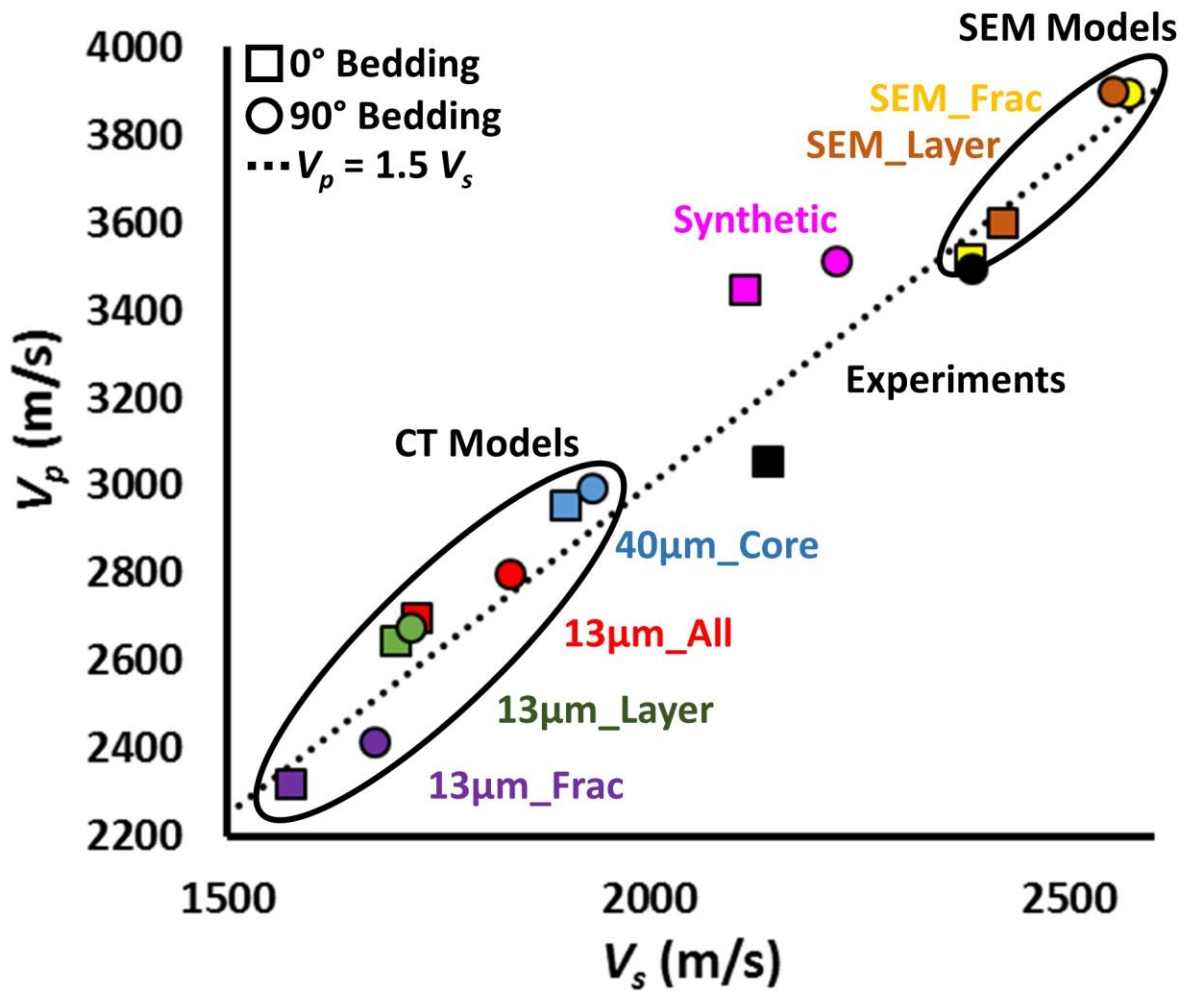


**Figure 9.** Comparison of  $P$ - and  $S$ -wave velocities obtained from experimental and numerical simulation results. Squares identify results obtained from wave propagation with layering at  $0^\circ$  and circles are for layering at  $90^\circ$ . The dashed line identifies the  $V_p/V_s$  ratio of 1.5.

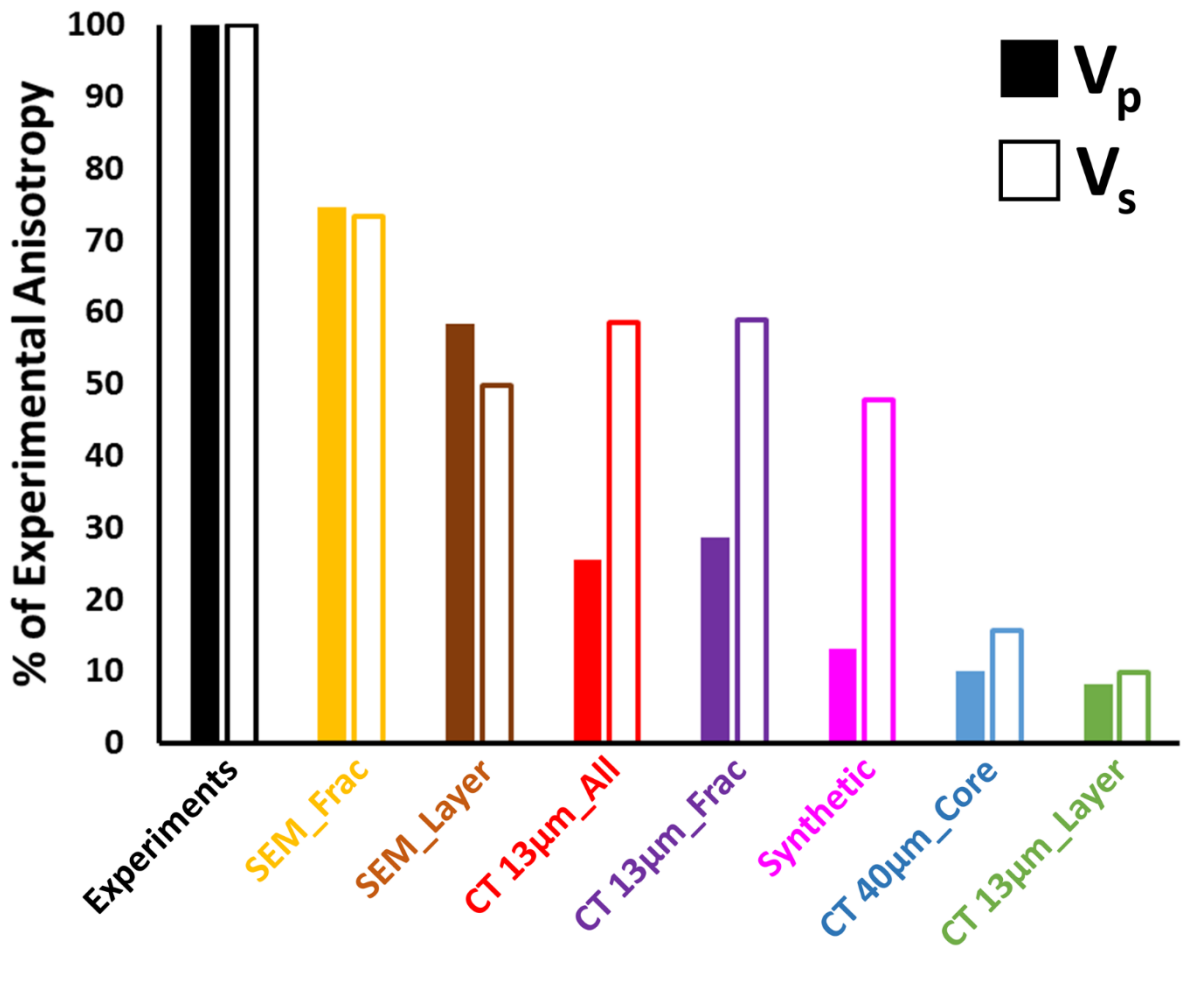


**Figure 10.** Comparison of the percent of  $P$ -wave (filled bar) and  $S$ -wave (empty bar) anisotropy from the various models normalized to the experimental measurements. Velocity anisotropy is defined as  $(V_{90^\circ} - V_{0^\circ}) / V_{0^\circ}$ , where  $V_{0^\circ}$  and  $V_{90^\circ}$  represent the wave velocities perpendicular and parallel to bedding, respectively.  $P$ - and  $S$ -wave velocity results and the absolute anisotropies are shown in Figure 9 and summarized in Table 3.

**Table 1.** Experimental measurements of  $P$ - and  $S$ -wave velocities on unconfined cores with bedding oriented at  $0^\circ$ ,  $45^\circ$ , and  $90^\circ$ . Velocities were used to calculate the Thomsen anisotropy parameters  $\epsilon$ ,  $\gamma$ , and  $\delta$ . The  $0^\circ$  and  $90^\circ$  measurements correspond to wave propagation perpendicular and parallel to bedding, respectively. For the  $45^\circ$  and  $90^\circ$  samples, perpendicular shear wave measurements  $V_{sa}$  and  $V_{sb}$  were oriented parallel and perpendicular to bedding, respectively, and had no preferred orientation for the  $0^\circ$  sample.

Bedding Orientation	$V_p$ (m/s)	$V_{sa}$ (m/s)	$V_{sb}$ (m/s)
$0^\circ$	3058	2150	2140
$45^\circ$	3295	2226	2105
$90^\circ$	3495	2382	2096
Thomsen Parameter	$\epsilon$	$\gamma$	$\delta$
	0.150	0.122	0.154

**Table 2.** Dominant minerals present in Mancos Shale and their respective mass density ( $\rho$ ), bulk ( $K$ ) and shear ( $\mu$ ) elastic moduli. In order from left to right, quartz, calcite, dolomite, kaolinite, illite, smectite, pyrite, orthoclase, albite. Endmember mineralogical composition (volume %) of quartz-rich (light) and clay-rich (dark) facies from SEM-EDS analysis. Total clay is the sum of kaolinite, illite, and smectite. Average density ( $\rho$ ) and effective bulk ( $K$ ) and shear ( $\mu$ ) elastic moduli are calculated from the volume fraction of each mineral and their mineral density or moduli. SEM images show that Mancos samples are comprised of approximately 64% Quartz-rich facies and 36% clay-rich facies.

Minerals	Qtz	Cal	Dol	Kaol	Ill	Smec	Pyr	Orth	Alb					
Mass Density $\rho$ (kg/m <sup>3</sup> )	2650	2710	2870	2440	2600	2400	5010	2640	2610					
Bulk Moduli $K$ (GPa)	37	70	80	46	45	9.5	140	65	55					
Shear Moduli $\mu$ (GPa)	41	28	45	22	20	6.9	125	30	30					
Facies Types	Volume % of Each Mineral										Total % Clay	Eff $K$ (GPa)	Eff $\mu$ (GPa)	Avg $\rho$ (kg/m <sup>3</sup> )
Quartz-rich	52.5	16.1	11.4	5.3	7.6	0.1	1.6	1.8	1.1		13	46.9	35	2663
Clay-rich	14.9	4.9	19.3	10.2	30	6	4.7	1.6	3.2		46.2	47	28	2614

**Table 3.** *P*- and *S*-wave velocities, volume average densities ( $\langle\rho\rangle$ ), and velocity anisotropies from experimental measurements (Exp) and simulation results. Velocity anisotropy is defined as  $(V_{90^\circ} - V_{0^\circ})/V_{0^\circ}$ , where  $V_{0^\circ}$  and  $V_{90^\circ}$  represent the wave velocities perpendicular and parallel to bedding, respectively. Models are shown in the following figures, 40  $\mu\text{m}$  resolution core-scale CT model (40 $\mu\text{m}$ \_Core) (Figure 4 and 6), synthetic layered model (Synthetic) (Figure 5), CT model at 13  $\mu\text{m}$  focused on layering (13 $\mu$ \_Layer) (Figure 6-C), fractures (13 $\mu$ \_Frac) (Figure 6-D), and encompassing both (13 $\mu$ \_All) (Figure 6-B), and SEM models focused on layering (SEM\_Layer) (Figure 7-D and E) and fractures (SEM\_Frac) (Figures 7-B and C). Densities do not vary for the 13 $\mu\text{m}$  CT or SEM models because the same physical model is used for wave propagation, but is rotated to simulate the  $0^\circ$  and  $90^\circ$  bedding/fractures. SEM models are constructed using the actual mineral velocities and densities from Wang et al. 2001 and Mavko et al 2009, whereas the CT models uses MVRH effective medium theory to determine effective elastic properties and velocities from the reference mineral properties and their volume fractions within each facies.

Dataset Name	$V_p$ (m/s)	$V_s$ (m/s)	$\langle\rho\rangle$ (kg/m <sup>3</sup> )	P-Anisotropy (%)	S-Anisotropy (%)
Exp_0°	3058	2150	2673	14.3%	10.8%
Exp_90°	3495	2382	2666		
CT 40 $\mu\text{m}$ _Core_0°	2956	1901	2477	1.4%	1.7%
CT 40 $\mu\text{m}$ _Core_90°	2998	1933	2484		
Synthetic_0°	3448	2113	2645	1.9%	5.2%
Synthetic_90°	3512	2222	2645		
CT 13 $\mu\text{m}$ _Layer_0°	2649	1700	2518	1.2%	1.1%
CT 13 $\mu\text{m}$ _Layer_90°	2680	1718	2518		
CT 13 $\mu\text{m}$ _Frac_0°	2320	1575	2543	4.1%	6.4%
CT 13 $\mu\text{m}$ _Frac_90°	2415	1675	2543		
CT 13 $\mu\text{m}$ _All_0°	2702	1725	2525	3.6%	6.3%
CT 13 $\mu\text{m}$ _All_90°	2800	1834	2525		
SEM_Layer_0°	3600	2420	2659	8.3%	5.4%
SEM_Layer_90°	3900	2550	2659		
SEM_Frac_0°	3520	2380	2574	10.7%	7.9%
SEM_Frac_90°	3895	2568	2574		